Article:

Krstajic, N., Hogg, R. and Matcher, S.J. (2011) Common path Fourier domain optical coherence tomography based on multiple reflections within the sample arm. Optics Communications, 284 (12). pp. 3168-3172. ISSN 0030-4018

https://doi.org/10.1016/j.optcom.2011.02.073

Common path Fourier domain optical coherence tomography based on multiple reflections within the sample arm

Nikola Krstajić[1a], Richard Hogg[1], Stephen J Matcher[2]

[1]*Department of Electronic Engineering, University of Sheffield, Mappin Street, Sheffield, S1 3JD, England, UK*
[2]*Department of Engineering Materials, University of Sheffield, Sir Robert Hadfield Building, Mappin Street, Sheffield, S1 3JD, England, UK*

Email: n.krstajic@physics.org

Short title: Common-path Fourier domain OCT

Keywords: biomedical optics, common path interferometry, low coherence interferometry, optical coherence tomography, Fourier domain optical coherence tomography

[a] Present address: Department of Physics, University of St Andrews, North Haugh, St Andrews, KY16 9SS, Scotland, UK.

ABSTRACT

We present a common path Fourier domain optical coherence tomography (FDOCT) setup where the reference signal arises from multiple reflections within the sample arm. Two configurations are demonstrated. The first is based on a reflective microscope objective while the second is based on a normal (refractive) microscope objective. The second configuration is effectively a Mireau interferometer. We present sensitivity analysis of these setups and images of *in vivo* skin. Advantages of both common path arrangements include: 1) the reference surface is not close to the sample surface while keeping the optical path lengths matched (so the additional interferometer is not needed) and 2) the user can independently control reference and sample arm power. Additionally, the configuration using the refractive objective ensures that the coherence gate and focus gate always match. A disadvantage is that the reference arm power in certain circumstances is not optimal (i.e. close to saturating the CCD). However, this issue can be removed by a light source of sufficient output power. We believe the idea is scalable and therefore of interest to endoscopy applications.

RESEARCH HIGHLIGHTS

- Multiple reflections within the sample arm can be beneficial.
- We demonstrate a novel common-path Fourier domain OCT based on Mireau interferometer.
- Potential applications are in endoscopy.

1 INTRODUCTION

Fourier domain optical coherence tomography (FDOCT) has been used extensively in many areas of epithelial tissue imaging [1, 2]. It is faster than the original optical coherence tomography technique (OCT), i.e. time domain optical coherence tomography (TDOCT), and has a sensitivity advantage [3-5]. Achieving ultrahigh resolution in OCT has been difficult to implement due to dispersion mismatch between sample and reference arm [6]. This is a special concern in endoscopy applications [7] where handling of long fibres exacerbates the problem. Apart from dispersion mismatch, problems arise in polarization fading and environmental effects such as temperature, pressure and fibre bending [8, 9]. All these problems are resolved if a common path interferometer is used. Broadly speaking, three architectures have been explored so far. In the first case, the reference arm is embedded in the sample arm and distant from the specimen. In this case, an additional interferometer (often called an autocorrelator) is required to bring together the distant arms of the first interferometer [10-17]. The second case uses a partially reflecting surface close to the specimen as the reference arm [18-23] thus obviating the need for the second interferometer. The third case incorporates a miniature interferometer close to tip of the fibre [19, 21].

All solutions have a common problem: reference arm and sample arm reflectance usually cannot be independently controlled (in fact it is possible in the first and third case mentioned above [24], but this has not been studied in detail). In this manuscript we present, to the best of our knowledge, a novel architecture that broadly falls in the second case above. We previously discussed a similar architecture for fibre sensing applications [25]. The reference arm is formed by engineering a doubly reflected signal from surfaces embedded in the signal path to the specimen. The main advantages of this setup are: 1) reference surface need not be close to sample surface; 2) tilting the reference surface can change the reference arm power independently of sample arm power; 3) the setups presented here do not need the additional interferometer.

Two common path configurations are demonstrated. The first uses a reflective objective while the second uses a normal refractive objective. In the second case, we intentionally use a refractive microscope objective corrected for visible light. This creates higher reflections off optical surfaces within the objective for near-infrared light (NIR). The second case is a Mireau interferometer widely used in surface metrology [26]. To the best of our knowledge, this is the first time it is applied to OCT. Setups presented have a merit in both FDOCT methods, namely spectrometer

based and swept source based OCT, although we show results only for spectrometer based system. This idea is applicable to configurations that use the additional interferometer such as the ones described in [10-17]. Additionally, it may be of interest in cases where interferometric phase retrieval is needed (e.g. in Doppler OCT [27] or spectral domain phase microscopy [28]). We believe the setups presented here are scalable and therefore applicable to endoscopy.

2 MATERIALS AND METHODS

The proposed setup is shown in figure 1. The light source used is Broadlighter D890-HP from Superlum, Russia. The total output of this source is 6mW from two multiplexed superluminescent diodes (SLEDs) with full width half maximum (FWHM) of 150 nm. The source is fed into the 3dB fibre coupler via a broadband isolator (IO-F-SLD150-895-APC, OFR, USA). Optical power after the fibre collimator in the sample arm is 1mW. The light from sample arm is detected by the spectrometer [2, 29]. The spectrometer has standard architecture [2, 30, 31], light exiting the fibre is collimated by an achromatic doublet lens (L_1 in figure 1) with focal length 50 mm. The expanded beam is dispersed by the blazed diffraction grating, 830 grooves per mm, (DG in figure 1, part number NT43-850, Edmund Optics, USA) and the first diffracted order is focused onto a CCD (Atmel Aviiva SM2CL2010, pixel size 10 μm, CCD integration time for imaging purposes was 400 μs and output charge amplifier gain was set to 0dB) using two identical focusing lenses (L_2 in figure 1). The two lenses are mounted together. Each is an achromat doublet, 200 mm in focal length and 50 mm in diameter making L_2 a compound lens with 100 mm focal length. Our experience is that two lenses improve the off-axis spot size, although the on-axis spot size is worse [31]. Spectrometer efficiency was measured to be 6%. This is a low value and we are investigating how to improve this.

Figure 2(a) shows a detailed view of the common path arm with reflective objective (referred to henceforth as configuration 1). The reference arm path goes from fibre collimator to S_2 and then reflects to S_1 while the sample arm path goes from fibre collimator to specimen. S_2 is tilted so that the reflected light is perpendicular to S_1 and therefore traces its way back to the fibre collimator. S_1 and S_2 are reflective neutral density filters (NDF). The reflectances of S_1 and S_2 are denoted R_{S1} and R_{S2} and their values are 36% and 50% respectively. The angles shown are exaggerated and the beams in practice largely overlap. S_2 is tilted by ~ 0.1° while S_1 is tilted by ~ 0.2°. The reference beam path is shown to pass twice through S_1 and S_2 in order to dispersion match the sample arm. So the beam needs to be carefully aligned in order to ensure the right surface is selected as the reference. As mentioned above, the microscope objective used in configuration 1 is reflective (Edmund Optics, USA,

part number NT59-888). The working distance of the reflective objective is 25 mm. A single axis galvanometer is placed between the objective and the specimen to ensure constant reference arm power throughout the scan. Although it was possible to place it prior to the objective, this complicated scanning.

Figure 2(b) shows a detailed view of the common path arm with refractive objective (referred to henceforth as configuration 2). Collimated light leaves the fibre collimator and is focused by the objective. A partially reflective surface (i.e. NDF) S is placed midway between the objective and the focus. With careful positioning the reflection from S will focus exactly on the tip of objective. As the objective is corrected for visible light, the reflection from the tip of the objective towards S is significant (~7%). As in figure 2(a) the reference beam path is shown to pass twice through S in order to dispersion match the sample arm. The beam from the fibre collimator needs to be centred on the microscope objective pupil in order to 1) ensure that the path is retraced back into the collimator, and 2) to provide maximum reflectance. This creates the reference arm within the common path arm. As mentioned previously, this configuration is known as Mireau interferometer. A single axis galvanometer is placed between the surface S and the specimen. The spacing between the galvanometer and the specimen is even more limited than in configuration 1. Note that configuration 2 ensures the reference and sample arm foci match automatically, so adjustment is minimal. This may be of use in optical coherence microscopy applications [32-34] if XY scanning is possible post-objective. The microscope objective used was Mitutoyo, ×10, part number 378-803-2. The working distance of the refractive objective is 33.5 mm.

The sensitivity of the system depends on total reflectance of the reference arm and can be calculated using the following equation (Eq. 6 from [5]).

$$\Sigma_{FDOCT} = \frac{\frac{1}{N}\left(\frac{\rho\eta\tau P_0}{h\nu_0}\right)^2 \gamma_s \gamma_r R_r}{\frac{1}{N}\left(\frac{\rho\eta\tau P_0}{h\nu_0}\right)\gamma_r R_r + \frac{1+\Pi^2}{2N\Delta\nu_{eff}}\left(\frac{\rho\eta\tau P_0 \gamma_r R_r}{h\nu_0}\right)^2 + \sigma_{receiver}{}^2}; \quad (1)$$

The terms in the above equation are as follows: γ_s and γ_r are fractions of input power exiting the interferometer from sample and reference arm respectively assuming perfect reflectors from sample and reference surfaces (both are affected by the coupling ratios of the fibre coupler and further attenuation due to multiple reflection in the NDF filters, see equations below), ρ is spectrometer efficiency (6%), η is detector quantum efficiency (40%), τ is CCD integration time (400 μs for images presented), h is Planck's constant, P_0 is the SLED ex-fibre power output (6 mW), Π is the polarization of the source (1 for both SLEDs), $\Delta\nu_{eff}$ is the linewidth of

the SLED (55.9 THz), N is the number of pixels used by spectra (1200) and $\sigma_{receiver}$ is the RMS receiver noise. Eq. (1) allows us to simulate expected sensitivities for various levels of reference arm power. The main term is R_r, reference arm reflectance which can be calculated for configuration 1 as:

$$R_r = (1 - R_{S1})^2 R_{S1} R_{S2}{}^2 \tag{2}$$

Where (1-R_{S1}) is the attenuation of the beam from the fibre collimator through the first surface S_1 (the value is squared due to double pass).

Configuration 2 has a similar relation:

$$R_r = (1 - R_{MO\_T})^2 R_S{}^2 R_{MO\_R} \tag{3}$$

Where R_S is the reflectance of surface S in figure 2(b), (1-R_{MO_T}) is the attenuation due to transmission through the microscope objective (45%), R_{MO_R} is the inherent reflectance of the tip of microscope objective (7%). Therefore in configuration 2 we rely on inherent reflectance of visibly corrected objectives in NIR, since objectives corrected for NIR are likely to have very low reflectances. In configuration 1 we have more control as the reference arm power is decided by the NDF reflectance we choose. This flexibility in configuration 2 would be available only if we were to design the microscope objective itself.

Eq. (1) is significantly affected by the fact that the power falling onto the sample is reduced by optical surfaces from the collimator to the sample. To take this into account γ_s from Eq. (1) for each configuration is given below:

$$\gamma_{s1} = \gamma_{IF} (1 - R_{S1})^2 (1 - R_{S2})^2 \tag{4}$$

$$\gamma_{s2} = \gamma_{IF} (1 - R_S)^2 (1 - R_{MO\_T})^2 \tag{5}$$

γ_{IF} is attenuation of input power due to 3dB fibre coupler (0.48^2 taking into account double pass). Eqs. (2)-(4) are calculated prior to using them in Eq. (1). They obviously will reduce sensitivity, but crucially, as we will show below, this need not be prohibitive. Note that we take $\gamma_r = \gamma_{IF}$ and calculate reference arm attenuation from Eqs. (2) and (3).

As mentioned previously, in both configurations the reference surface is not close to the specimen surface. Furthermore, the tilting of relevant surfaces can change the reference arm power level independently of the sample arm power. This is important for optimizing the sensitivity of the system. This is not novel in itself, but common-path systems usually do not allow for this flexibility. Lastly, in configuration 2 the reference path length and objective focus match automatically, so once aligned readjustments are minimal.

3 RESULTS

Figure 3(a) shows theoretical sensitivity as a function of R_{S1} and R_{S2} (assumed to be the same for simplicity) for configuration 1 while figure 3(b) shows the theoretical sensitivity as a function of R_S for configuration 2. This effectively gives the sensitivity as the function of reference arm power, as this can be directly calculated from equations (2) and (3). The main effect of increasing the reference arm power (R_{S1} and R_{S2} in configuration 1 or R_S in configuration 2) is that at a certain point the power falling onto the specimen becomes too small (and this light is further attenuated on the way back). One advantage of the arrangements presented here is that a given reference arm power can be reduced by tilting either surfaces S_1 and S_2 in configuration 1 or surface S in configuration 2. Possible improvements to our setup include using a circulator instead of an isolator to maximize power efficiency. However, broadband circulators are hard to obtain, so we were not able to implement this step. Increasing CCD integration time from 40 μs to 400 μs improves the sensitivity to a maximum theoretical value above 100dB for configuration 1. The problem remains for fast imaging (40 μs integration time or less). Sensitivity in this case is not satisfactory, but can be attained by a more powerful light source and improvements in our spectrometer (for example spectrometer efficiency is 6% and should be higher, at least 20% to 30% [31, 35]).

Figure 4(a) shows spectral fringes (after background subtraction) with mirror as the specimen. Figure 4(b) shows the point spread function (PSF) with a resolution of approximately 4 μm in air which is close to theoretical value 3.7 μm (obtained by calculating the coherence function of the source spectra). Figure 4(b) is a Fourier transform of figure 4(a) (after performing k-space interpolation on figure 4(a)). The results in fig 4 were done using configuration 1. Similar results were obtained with configuration 2. Lateral resolution for both configurations was 13 μm.

Figure 5 shows the theoretical reference arm reflectance power as a function of inline surface reflectance $R_{S1} = R_{S2}$ for configuration 1 and R_S for configuration 2. CCD saturation powers at 40 μs and 400 μs are 60 μW and 6 μW respectively. Figure 5 needs to be compared with figure 3 in order to find optimal reflectance of NDFs. The aim is to have enough reference arm power to saturate the CCD (see figure 5) while achieving optimal sensitivity (see figure 3). For example, $R_{S1} = R_{S2} = 20\%$ in configuration 1 should give optimal sensitivity and should saturate the CCD at 400 μs integration time. However, we could not achieve CCD saturation in practice for these reflectances, probably due to low quality of the fibre collimator employed. Raising R_{S1} and R_{S2} to 36% and 52% respectively achieved CCD saturation for configuration 1. Note that further increase in reflectances for configuration 1 becomes

counterproductive and at R_{S1} = R_{S2} = 65% the total reference arm reflectance decreases due to decrease in the beam power reaching surface S_2. For configuration 2, R_S = 50% should provide optimal sensitivity and reference arm power (R_{MO_R} was measured to be 7%). However, with the reflectance R_S = 45% the reference arm power reached only 20% of maximum CCD intensity, at 400 μs integration time. For simulation purposes, we assumed that the reflection from surface S falls onto the tip of the objective and reflects perfectly backwards onto S. The problem is that the tip of the objective is curved and it is hard to locate the place where reflections fit the simulation. Further improvements in the alignment should improve the situation. Note that increasing the output power to 10 mW scales all the graphs by 10dB, so higher power allows using lower reflectance NDFs to achieve optimal reference arm power for sensitivity.

Figure 6 shows sample images of *in vivo* skin with configuration 1 and configuration 2. CCD integration time was 400 μs for both configurations. The skin images show clear stratum corneum and lower layers of epidermis. Both images display a vertical artefact (red arrows) which is probably a motion artefact. The sensitivity of configuration 1 was measured to be 89dB while for configuration 2 it was 82dB and these values are about 10 dB lower than ones predicted from theory (see figure 3). See the section below for a discussion regarding these results.

4 DISCUSSION

Several interesting points regarding the arrangements presented here need to be mentioned. The light exiting the collimator is never perfectly collimated so part of the beam is lost for long optical path lengths. By introducing intermediate surfaces the dispersion is not perfectly matched as the reference arm and sample arm optical path may traverse intermediate surfaces a different number of times. Further complications arise when considering reflections from the inner and outer surface of any of the intermediate surfaces. In configuration 1 we use reflective objective and therefore the dispersion mismatch would not be a problem even with a separate reference arm. As an aside, we think that applying reflective objectives to OCT may need more attention for this reason as well as for their flat response in the NIR range. One difficulty in using reflective objectives in OCT is that it is harder to apply them to beam scanning configurations for lateral scans above 2 mm.

The thickness of intermediate surfaces needs to be greater than depth studied as well. This avoids multiple images within the same cross sectional scan. Autocorrelation artefact is visible along the middle of the skin image in figure 6 for configuration 2. This is probably due to a multiply reflected image of the surface

within the microscope objective. Alternative solutions include introducing NDFs with non-parallel surfaces, i.e. wedges.

Single axis galvanometer is placed post-objective in both configurations and this limits the size of the lateral scan. We were able to perform 2 mm scans relatively easily. A further limitation is that the galvanometer is close to the specimen (>5 mm) which increases the possibility of damaging the galvanometer. Note that an improvement to the setup would be to design a custom refractive microscope objective that includes the multiply reflected signal in the design. Currently, in order to enable pre-objective scanning, a specially curved surface for each objective would need to be designed. Although possible, one needs a detailed surface curvature of commercial microscope objectives, which are usually not available.

Multiple reflections are mostly a nuisance in optical designs, especially so in interferometric setups, and this is due to their increased sensitivity [36]. Here, we have tried to show that one can take advantage of them if their presence is considered at design stage. Furthermore, if one designs with multiple reflections in mind then there are many other configurations to consider.

Despite the issues mentioned above, the implementation shown here is very versatile and the skin images are good. In an endoscopy arrangement, the GRIN lens is usually attached to the distal end of the fibre. Partial reflector could be mounted after the GRIN lens at half of the working distance. The implementation for partial reflector could be a wedge shaped film in order to minimise coherent artefacts. The main engineering problem would be to ensure correct alignment of the partial reflector and the stiffness of the whole unit.

5 CONCLUSION

We have shown two simple common path solutions applied to spectrometer based FDOCT. The arrangements are applicable to swept-source based OCT systems as well, provided sufficient reference arm power is available from the multiply reflected reference arm. Although increasing the reference arm power by increasing inline reflectances reduces power falling onto the specimen, we have the control to reduce the reflectance if the power source has high output power (such is the case in configuration 1). We believe the results presented are of interest for endoscopy applications.

6 ACKNOWLEDGEMENTS

We would like to thank Zhengai Lu, Deepa Kamath Kasaragod and James Jacobs for many fruitful discussions. The CameraLink side of CCD software was

written by Sergey Gangnus. We thank Mario Giardini from the University of St Andrews for ideas regarding the endoscopy implementation. The study was funded by United Kingdom Engineering and Physical Sciences Research Council grant, number EP/H008004/1. NK would like to thank Cathy Shields for carefully reading the original manuscript.

BIBLIOGRAPHY

[1] W. Drexler, J.G. Fujimoto, Optical coherence tomography : technology and applications, Springer, Berlin; New York, 2008.
[2] M. Wojtkowski, High-speed optical coherence tomography: basics and applications, Appl. Opt., 49 (2010) D30-D61.
[3] M.A. Choma, M.V. Sarunic, C.H. Yang, J.A. Izatt, Sensitivity advantage of swept source and Fourier domain optical coherence tomography, Optics Express, 11 (2003) 2183-2189.
[4] J.F. de Boer, B. Cense, B.H. Park, M.C. Pierce, G.J. Tearney, B.E. Bouma, Improved signal-to-noise ratio in spectral-domain compared with time-domain optical coherence tomography, Opt. Lett., 28 (2003) 2067-2069.
[5] R. Leitgeb, C. Hitzenberger, A. Fercher, Performance of fourier domain vs. time domain optical coherence tomography, Opt. Express, 11 (2003) 889-894.
[6] W. Drexler, Ultrahigh-resolution optical coherence tomography, Journal of Biomedical Optics, 9 (2004) 47-74.
[7] Z. Yaqoob, J. Wu, E.J. McDowell, X. Heng, C. Yang, Methods and application areas of endoscopic optical coherence tomography, J Biomed Opt, 11 (2006) 063001.
[8] K.T.V. Grattan, T. Sun, Fiber optic sensor technology: an overview, Sensors and Actuators A: Physical, 82 (2000) 40-61.
[9] D. Stowe, D. Moore, R. Priest, Polarization fading in fiber interferometric sensors, Quantum Electronics, IEEE Journal of, 18 (1982) 1644-1647.
[10] F. Feldchtein, J. Bush, G. Gelikonov, V. Gelikonov, S. Piyevsky, Cost effective, all-fiber autocorrelator based 1300 mn OCT system, Coherence Domain Optical Methods and Optical Coherence Tomography in Biomedicine IX, 5690 (2005) 349-355.
[11] H.D. Ford, R.P. Tatam, Fibre imaging bundles for full-field optical coherence tomography, Measurement Science and Technology, 18 (2007) 2949.
[12] J.H. Han, X. Liu, C.G. Song, J.U. Kang, Common path optical coherence tomography with fibre bundle probe, Electronics Letters, 45 (2009) 1110-1111.
[13] X. Liu, X.L. Li, D.H. Kim, I. Ilev, J.U. Kang, Fiber-optic Fourier-domain common-path OCT, Chinese Optics Letters, 6 (2008) 899-901.
[14] U. Sharma, N.M. Fried, J.U. Kang, All-fiber common-path optical coherence tomography: sensitivity optimization and system analysis, Selected Topics in Quantum Electronics, IEEE Journal of, 11 (2005) 799-805.
[15] U. Sharma, J.U. Kang, Common-path optical coherence tomography with side-viewing bare fiber probe for endoscopic optical coherence tomography, Review of Scientific Instruments, 78 (2007).
[16] U. Sharma, J.U. Kang, Simultaneous imaging and measurement of tensile stress on cornea by using a common-path optical coherence tomography system with an external contact reference, Chinese Optics Letters, 6 (2008) 910-912.
[17] K. Zhang, E. Katz, D.H. Kim, J.U. Kang, I.K. Ilev, Common-path optical coherence tomography guided fibre probe for spatially precise optical nerve stimulation, Electronics Letters, 46 (2010) 118-119.
[18] A.H. Bachmann, R. Michaely, T. Lasser, R.A. Leitgeb, Dual beam heterodyne Fourier domain optical coherence tomography, Optics Express, 15 (2007) 9254-9266.
[19] R.A. Leitgeb, R. Michaely, T. Lasser, S.C. Sekhar, Complex ambiguity-free Fourier domain optical coherence tomography through transverse scanning, Opt. Lett., 32 (2007) 3453-3455.

[20] K.M. Tan, M. Mazilu, T.H. Chow, W.M. Lee, K. Taguchi, B.K. Ng, W. Sibbett, C.S. Herrington, C.T.A. Brown, K. Dholakia, In-fiber common-path optical coherence tomography using a conical-tip fiber, Opt. Express, 17 (2009) 2375-2384.
[21] A.R. Tumlinson, J.K. Barton, B. Povazay, H. Sattman, A. Unterhuber, R.A. Leitgeb, W. Drexler, Endoscope-tip interferometer for ultrahigh resolution frequency domain optical coherence tomography in mouse colon, Opt. Express, 14 (2006) 1878-1887.
[22] A.R. Tumlinson, B. Povazay, L.P. Hariri, J. McNally, A. Unterhuber, B. Hermann, H. Sattmann, W. Drexler, J.K. Barton, In vivo ultrahigh-resolution optical coherence tomography of mouse colon with an achromatized endoscope, Journal of Biomedical Optics, 11 (2006) 064003-064008.
[23] A.B. Vakhtin, D.J. Kane, W.R. Wood, K.A. Peterson, Common-Path Interferometer for Frequency-Domain Optical Coherence Tomography, Appl. Opt., 42 (2003) 6953-6958.
[24] J.U. Kang, A. Rodriguez, Fourier Domain Common-Path Fiber OCT with Tunable Reference: Analysis and Optimization, 2007 Conference on Lasers & Electro-Optics/Quantum Electronics and Laser Science Conference (Cleo/Qels 2007), Vols 1-5, (2007) 1890-1891.
[25] N. Krstajić, D. Childs, R. Smallwood, R. Hogg, S.J. Matcher, Common path Michelson interferometer based on multiple reflections within the sample arm: sensor applications and imaging artefacts, Measurement Science and Technology, 22 (2011).
[26] D.J. Whitehouse, Surface metrology, Measurement Science and Technology, 8 (1997) 955.
[27] Z. Chen, J. Zhang, Doppler Optical Coherence Tomography, in: Optical Coherence Tomography, 2008, pp. 621-651.
[28] M.A. Choma, A.K. Ellerbee, C. Yang, T.L. Creazzo, J.A. Izatt, Spectral-domain phase microscopy, Opt. Lett., 30 (2005) 1162-1164.
[29] J.F. Boer, Spectral/Fourier Domain Optical Coherence Tomography, in: W. Drexler, J.G. Fujimoto (Eds.) Optical Coherence Tomography, 2008, pp. 147-175.
[30] M. Wojtkowski, R. Leitgeb, A. Kowalczyk, T. Bajraszewski, A.F. Fercher, In vivo human retinal imaging by Fourier domain optical coherence tomography, Journal of Biomedical Optics, 7 (2002) 457-463.
[31] M. Wojtkowski, V. Srinivasan, T. Ko, J. Fujimoto, A. Kowalczyk, J. Duker, Ultrahigh-resolution, high-speed, Fourier domain optical coherence tomography and methods for dispersion compensation, Opt. Express, 12 (2004) 2404-2422.
[32] A.D. Aguirre, J.G. Fujimoto, Optical Coherence Microscopy, in: Optical Coherence Tomography, 2008, pp. 505-542.
[33] J.A. Izatt, M.R. Hee, G.M. Owen, E.A. Swanson, J.G. Fujimoto, Optical coherence microscopy in scattering media, Optics Letters, 19 (1994) 590-592.
[34] A.G. Podoleanu, G.M. Dobre, D.A. Jackson, En-face coherence imaging using galvanometer scanner modulation, Optics Letters, 23 (1998) 147-149.
[35] N. Nassif, B. Cense, B. Park, M. Pierce, S. Yun, B. Bouma, G. Tearney, T. Chen, J. de Boer, In vivo high-resolution video-rate spectral-domain optical coherence tomography of the human retina and optic nerve, Opt. Express, 12 (2004) 367-376.
[36] P.C.D. Hobbs, Building electro-optical systems making it all work, second edition, Wiley, Hoboken, N.J., 2009.

FIGURES CAPTIONS

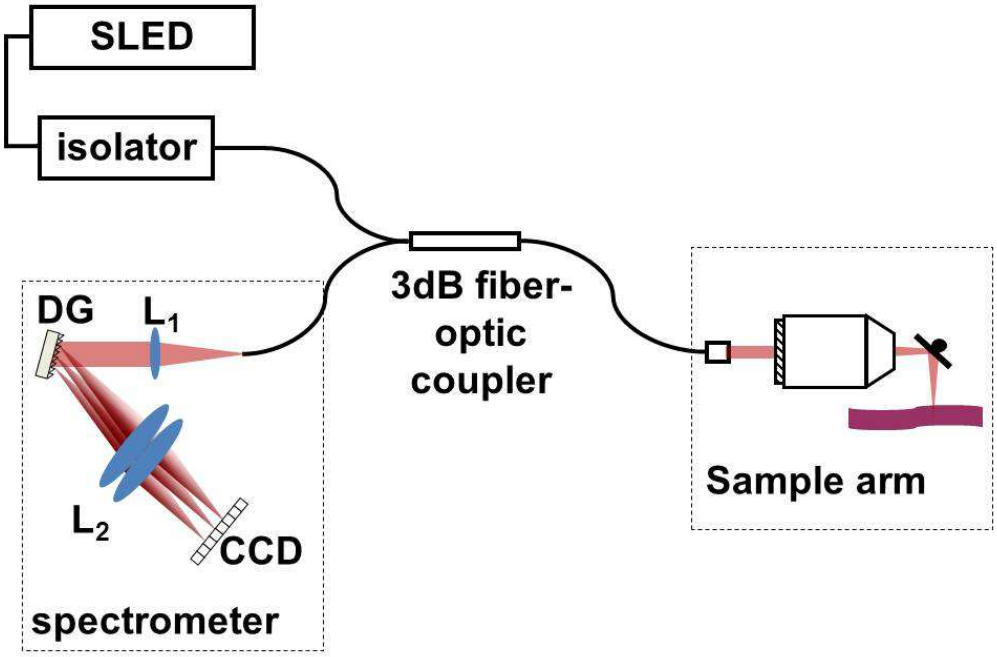

Figure 1. FDOCT diagram. Details of two configurations in the sample arm are given in figure 2. M – mirror, DG – diffraction grating, L_1 and L_2 – lenses, SLED – superluminescent diode

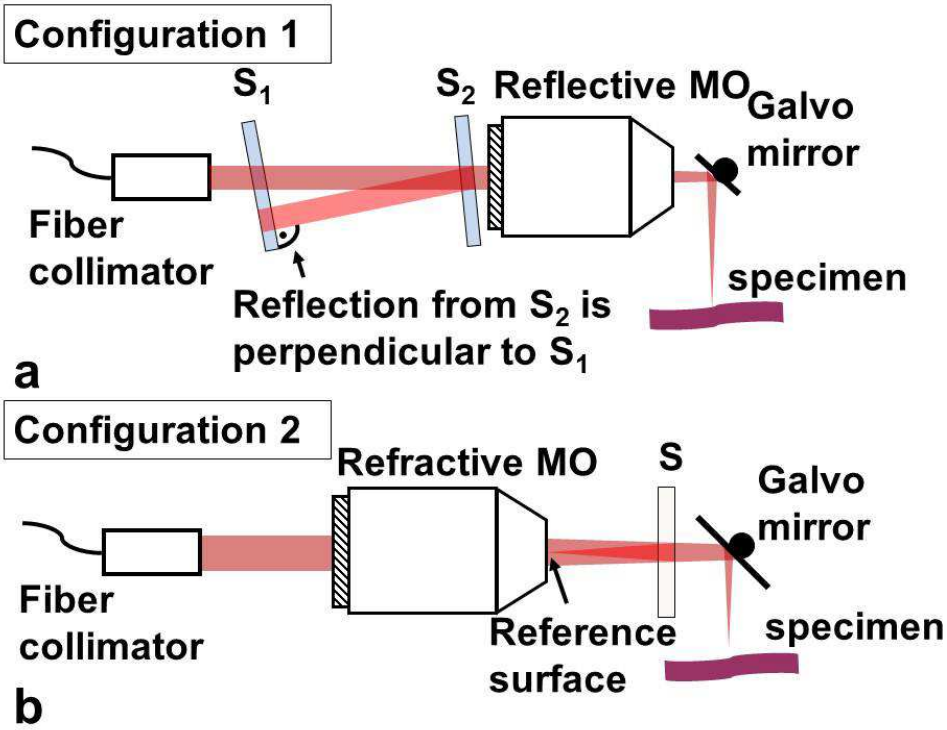

Figure 2 (a) shows the configuration based on reflective objective (configuration 1) and (b) shows the configuration based on refractive objective (configuration 2). Doubly reflected surfaces are placed pre-objective in (a) while in (b) the doubly reflected surface S is post-objective. The tilt of S_1 and S_2 in (a) is exaggerated for demonstration (the angles are 0.2 and 0.1 degrees for S_1 and S_2 respectively).

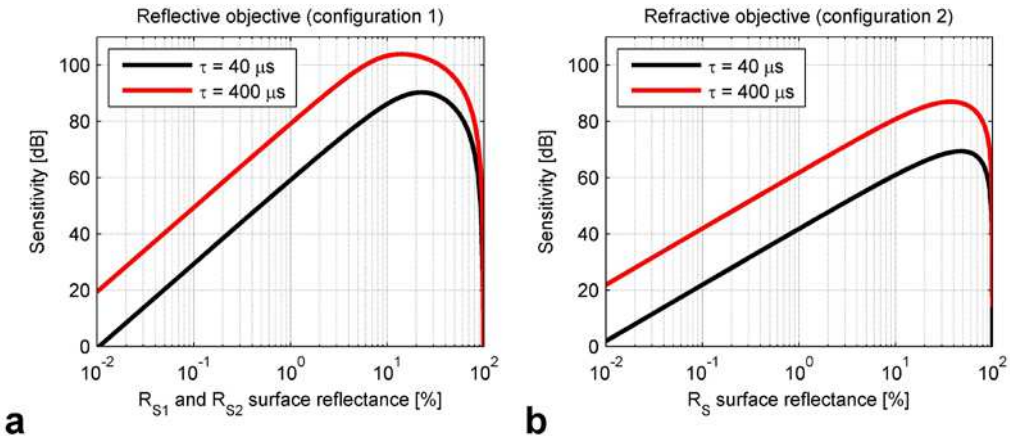

Figure 3 (a) shows the sensitivity dependence on reflectance of surfaces S_1 and S_2 for configuration 1 while (b) shows the sensitivity dependence on reflectance of surface S for configuration 2.

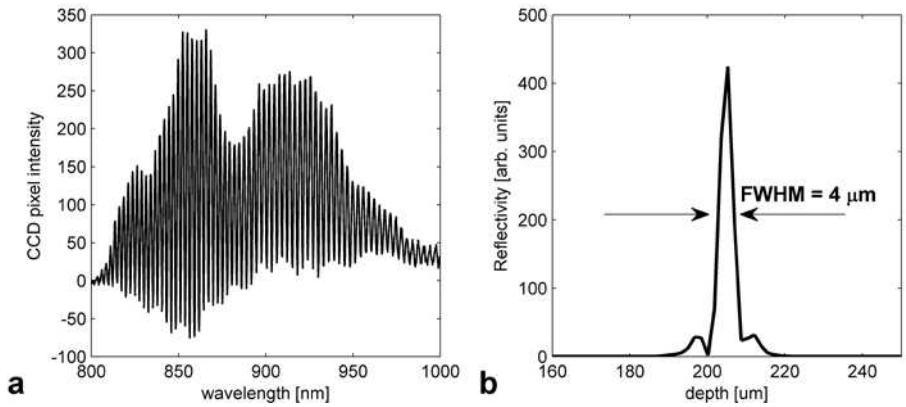

Figure 4. (a) shows sample fringe pattern generated from mirror in configuration 1 (after background subtraction); (b) shows FWHM to be 4 μm (in air) (theoretical value is 3.7 μm).

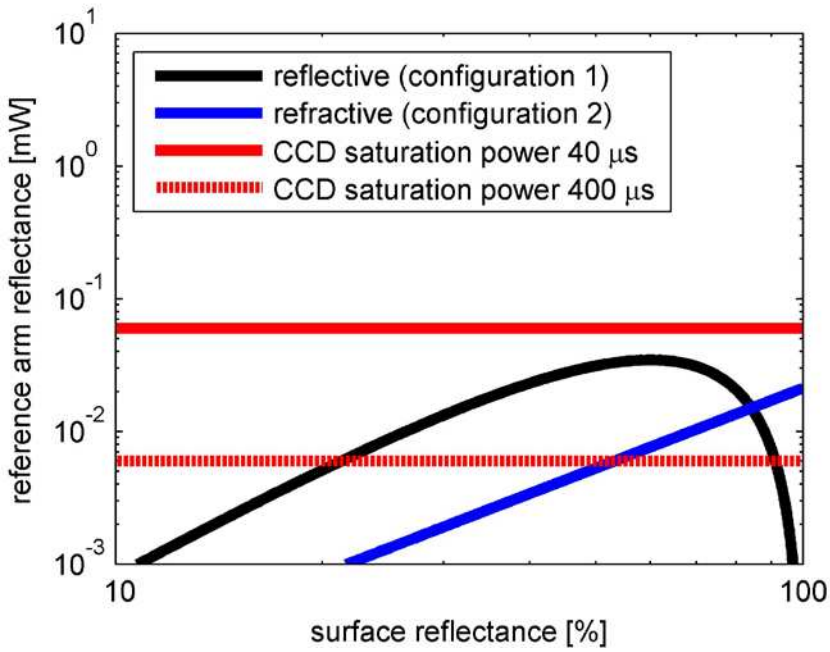

Figure 5. Total reference arm power is higher for configuration 1. Note that surface reflectance refers to R_{S1} and R_{S2} in case of configuration 1 or R_S in case of configuration 2.

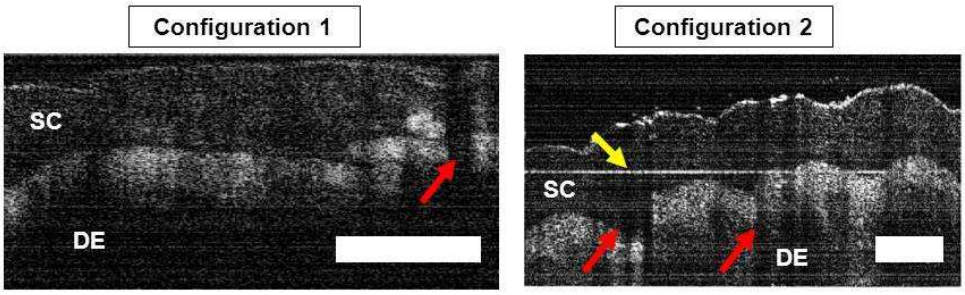

Figure 6. Palmar skin from small finger is shown for configuration 1 and 2. Bar is ~200 μm. SC: stratum corneum, DE: dermis, yellow arrow points to autocorrelation artefact while red arrows point to vertical artefacts.